IN-25
372733

Oxidative Attack of Carbon/Carbon Substrates through Coating Pinholes

Nathan S. Jacobson[1], Todd Leonhardt[2], Donald Curry[3]
and Robert A. Rapp[4]

[1]NASA Lewis Research Center, Cleveland, OH
[2]NYMA, Inc., NASA Lewis Research Center Group, Cleveland, OH
[3]NASA Johnson Space Center, Houston, TX
[4]The Ohio State University, Dept. of Materials Science and Engineering, Columbus, OH

Abstract

A critical issue with oxidation protected carbon/carbon composites used for spacecraft thermal protection is the formation of coating pinholes. In laboratory experiments, artificial pinholes were drilled through SiC-coatings on a carbon/carbon material and the material was oxidized at 600, 1000, and 1400°C at reduced pressures of air. The attack of the carbon/carbon was quantified by both weight loss and a novel cross-sectioning technique. A two-zone diffusion control model was adapted to analyze this problem. Agreement of the model with experiment was reasonable at 1000 and 1400°C; however results at lower temperatures show clear deviations from the theory suggesting that surface reaction control plays a role.

Introduction

One dimensional

Carbon/carbon composites are lightweight with desirable mechanical properties at high temperatures. Of course, the reactivity of carbon in oxidizing atmospheres at high temperatures is the drawback. To this end, several oxidation-protection schemes have been developed. These include silicon carbide (SiC) with an over-coating of glass (1), SiC with various boron-containing compounds, and SiC with an over-coating of refractory oxides (2). The SiC/glass protection scheme shown in Figure 1 was relevant to the current study.

Regardless of the specific coating scheme, pinholes in the protective coating are a potential problem (3). These provide a path for oxygen to attack the carbon/carbon with formation of a cavity below the coating and eventual consumption of the underlying carbon/carbon. The purpose of this paper is to report observations of these cavities and present a model for their formation.

Carbon oxidation has been extensively studied (4,5). At high temperatures, carbon oxidizes primarily to CO(g) when the supply of oxygen is limited:

$$C(s) + \tfrac{1}{2} O_2(g) = CO(g) \qquad (1)$$

However air contains both $O_2(g)$ and $CO_2(g)$, which are not thermochemically compatible with CO(g). For this reason, there is an additional reaction step in carbon oxidation:

$$CO(g) + \tfrac{1}{2} O_2(g) = CO_2(g) \qquad (2)$$

The gas-phase diffusion-controlled oxidation of a carbon substrate through pores has been treated by several investigators for a variety of applications. These applications include the burnout of carbon between two alumina plates (6), the oxidation of TaC (7,8), oxidation of carbon fiber coatings in composites (9-11), and the oxidation of carbon in an alumina matrix (12). In the case of TaC oxidation, a porous oxide forms as an outer layer and oxidation occurs through the pores. In all four cases, the process is described by two regions, as shown schematically for pinhole oxidation of SiC-coated carbon/carbon in Figure 2. Flux equations are set up for each region, together with boundary conditions. Solutions to the diffusion equation lead to the carbon consumption rate. The major difference between the treatments is the selection of a suitable geometry and coordinate system.

In this paper we will focus on SiC-protected carbon/carbon. After about twelve flights small (< 1 mm) pinholes have been observed on the wing-leading-edge of the US space shuttle orbiter (3). This study is part of a larger program to understand the origin of these pinholes and to model the potential damage to the underlying carbon/carbon.

The experiments reported here were done at reduced pressures to model the atmosphere entry environment. These experiments were then modeled with adaptations of the well-established models described above. Although the experiments are with SiC-coated carbon/carbon and emphasize re-entry applications, these experiments and models are quite general and apply to other coatings of carbon/carbon in other applications.

Experimental

Carbon/Carbon Material

The material is the same as that used for the wing-leading-edge of the shuttle (Lockheed Martin Vought Systems, Dallas, TX). It is shown schematically in Figure 1 and described in more detail in reference (13). This material consists of layers of a graphitized rayon fabric, which are repeatedly impregnated with a liquid carbon precursor to fill the voids and then the precursor is converted to carbon by pyrolysis. A diffusion conversion coating of silicon carbide is then grown on this substrate at high temperatures by a siliconizing pack cementation process. Next a coating of tetraethyl orthosilicate (TEOS) is applied via a vacuum impregnation to form silicon dioxide on the surface to plug surface cracks and fissures. The final coating is a "Type A" sealant which consists of sodium silicate and small particles and fibers of SiC. The difference in thermal expansion of the SiC coating and the carbon/carbon substrate leads to cracks in the SiC and the fluid glass from the TEOS and Type A coatings is intended to fill these cracks. Samples in the form of 2 cm diameter disks were used for the laboratory furnace study. Larger disks, about 7 cm in diameter, were used for the arc-jet study.

Artificial pinholes were made through the glass and SiC of this material with an ultrasonic drill (Sonic-Mill, Albuquerque, NM). Figure 3(a) shows a top view of a carbon/carbon disk with drilled holes and Figure 3(b) shows a cross-section of a hole close to the SiC interface with the carbon/carbon. The procedure to produce this cross-section is described below. For the furnace specimens a grid of nine holes was drilled; for the arc-jet specimen, a grid of six holes was drilled.

Oxidation Treatments

For the furnace exposure, disks without pinholes were first tested at each temperature to determine the extent of coating loss and general outgassing under the test conditions. The weight loss data are shown in Table I. Two to four replicate runs were done for each condition. The weight losses for samples with pinholes were corrected so that the weight loss per pinhole reflects only the oxidation of the carbon/carbon.

The test specimens were heat treated in a horizontal furnace with molybdenum disilicide elements at a reduced pressure of air, to simulate a portion of the entry atmosphere. A schematic diagram of the apparatus is shown in Figure 4. Pressure was monitored with a capacitance manometer and controlled with a needle valve. Temperature was monitored by a Pt/Pt-Rh thermocouple adjacent to the samples. Table II lists the experimental exposures.

After exposure, the samples were analyzed both from weight change data and microstructure. A simple weight change indicated the amount of carbon oxidized. Only one specimen (with nine holes) was run per condition and the corrected weight loss per sample is shown in Table II. The error on these numbers reflects only the weight loss from the blanks (Table I), where multiple specimens were run.

The samples were also sectioned, ground, and examined in cross-section. This was done by first vacuum infiltrating and mounting the specimens in epoxy. Then the specimens were sectioned with a slow-speed diamond saw, taking care not to cut through the pinholes. Each section was then re-mounted and ground until a groove appeared corresponding to a pinhole. These were subsequently ground to 20 μm diamond to expose the structure around the pinhole.

In addition, one specimen was oxidized in the arc-jet facility at NASA Johnson Space Center. This disk with pinholes exhibited more attack than those run in the furnace. The arc-jet exposure was at 1538°C and 0.05 atm for a total time of 3.5 hr. The atmosphere is air with substantial amounts of atoms and ions formed in the arc. Tests were interrupted for weighing at regular intervals.

In most cases, the carbon/carbon below the pinhole oxidized to form an approximate semi-circular cross-section, indicating that the cavity resembles a hemisphere. This geometry was incorporated into the model.

Results

A summary of the experimental data is shown in Table II. Weight losses per pinhole were determined by taking the total weight loss and dividing by the number of pinholes through which oxidation occurred. Generally this was nine, but in some instances the drilled hole did not reach the carbon/carbon or else the hole was clogged. Representative micrographs are shown in Figures 5-8 from which a number of important observations can be drawn. At 600°C, there appears to be no attack at this scale; however there is some weight loss. The carbon/carbon

substrate contains two forms of carbon--the fibers and the matrix material. It is well-known that the matrix material oxidizes more rapidly than the fibers. The 600°C oxidative weight loss likely reflects the oxidation of the matrix material, which is not be evident in the low-magnification cross-section. Figure 9 is a micrograph of the carbon/carbon substrate (without SiC/glass coating) oxidized at 600°C. This illustrates the preferential attack of the matrix material.

At higher temperatures, there is clearly more attack and the region below the pinhole exhibits a bowl-like appearance. At 1600°C, substantial attack of the SiC coating is observed in addition to oxidation of the carbon/carbon can be seen, as shown in Figure 8. No attempt was made to model the 1600°C exposure, since the coating system was also attacked.

One sample was exposed in an arc-jet (sample AJ1 in Table II). Figure 10 is a plot of weight loss of this specimen as a function of time. This reported total weight loss reflects weight loss from both the coating and oxidation of the carbon/carbon. Figures 10 and 11 and Table II indicate substantial attack of the carbon/carbon under these conditions.

For the furnace exposures at 1000°C and 1400°C and the arc-jet exposure, we assumed the attacked region was a hemisphere and calculated the weight loss due to formation of the hemisphere. Thus the weight loss, W, was calculated from:

$$W = 4\,\pi/6\,(2A/\pi)^{3/2}\,\rho = 1.45\,A^{3/2} \qquad (3)$$

Here A is the cross-sectional oxidized area below the pinhole and ρ is the density of carbon/carbon taken to be 1.362 gm/cc. The area was measured by the standard technique of counting squares on graph paper. Since the oxidized area was not a perfect hemisphere, measurement of an area should be more accurate than measuring a single radius or average of several radii. The calculated weight changes are also shown in Table II. For 1000 and 1400°C the weight changes calculated in this way and those determined by direct weighing show reasonable agreement. The measured weight changes were nearly always greater; they include preferential oxidation of the carbon matrix material, which may extend well into the matrix but may not be observed in the optical micrographs. Likewise, any offset of the cross-sections from the centerline can only result in a lower area.

Model

General Approach

As mentioned, this oxidation process can be described by a model of countercurrent diffusion in a pore. Following Bernstein and Koger (6), the basic assumptions in this model are:

1. The reaction rate is controlled by diffusion of the reactants and products within the pore.
2. All gases act ideally.
3. The gas phase diffusion coefficients are independent of concentration.
4. The oxidation process is described by gaseous diffusion in two regions, corresponding to the diagram in Figure 2(b). —— YOU SHOULD MENTION HERE THAT THE MODELED PROCESS IS ONE DIMENSIONAL

The approach here is similar to that used by other investigators. Fluxes, J_i, are defined for each region according to:

$$J_i = - D_{i,eff}\left(\frac{\partial c_i}{\partial x}\right) + c_i \sum_{j=1}^{n} J_j \qquad (4)$$

Here $D_{i,eff}$ is the gas phase interdiffusion coefficient of the ith component, c_i is its concentration, and x is the distance from the carbon/gas interface. The first term in equation (4) is the standard Fickian diffusion term, the second term is the convection term required when additional gas molecules are created at the boundary between Regions I and II. Gas-phase interdiffusion coefficients are calculated from the standard Chapman-Enskog relationship (14):

$$D_{i-N_2} = 0.001853\left(\frac{1}{M_i} + \frac{1}{M_{N_2}}\right)^{1/2} T^{3/2}\left(\frac{1}{P\sigma_{A-B}^2\Omega}\right) \qquad (5)$$

Here M_i are the masses of the subscripted molecule (in grams/mole), T is the absolute temperature, P is the total pressure (in atm), σ_{A-B} is the average of the two diameters, and Ω is the collision integral determined from standard tabulations (15, 16). Table III lists the calculated diffusivities for the conditions of interest in this study.

Calculation of Location of Region (I)/Region (II) Boundary

First consider Region (I), which has only CO_2 and O_2 counterdiffusing through nitrogen. These fluxes are described by:

$$J^{I}_{O_2} = -\frac{D_{O_2} c^{o}_{O_2}}{L - x_f} \tag{6}$$

$$J^{I}_{CO_2} = -\frac{D_{CO_2} c^{*}_{CO_2}}{L - x_f} \tag{7}$$

The parameters c, L, and x_f are defined in Figure 2(b). Note that these fluxes do not include a convection term, since the diffusion fluxes of O_2 and CO_2 molecules are of equal and opposite magnitude. We can obtain $c^{*}_{CO_2}$:

$$c^{*}_{CO_2} = \frac{c^{o}_{O_2} D_{O_2}}{D_{CO_2}} \tag{8}$$

Next consider Region II, which contains both CO_2 and CO. Now we have a convection term, since for the diffusion flux of CO is twice that for CO_2:

$$J^{II}_{CO} = -2 J^{II}_{CO_2} \tag{9}$$

The flux of CO_2 is given by equation (4):

$$J^{II}_{CO_2} = -D_{CO_2}\left(\frac{\partial c_{CO_2}}{\partial x}\right) - \frac{c_{CO_2} J^{II}_{CO_2}}{c_T} \tag{10}$$

This can be rearranged and integrated to give:

$$J^{II}_{CO_2} = -\left(\frac{c_T D_{CO_2}}{x_f}\right) \ln\left[\frac{\left(c_T + c^{*}_{CO_2}\right)}{\left(c_T + c^{**}_{CO_2}\right)}\right] \tag{11}$$

Because $c^{\bullet}_{CO_2} \rangle\rangle c^{\bullet\bullet}_{CO_2}$ and we also have an expression for $c^{\bullet}_{CO_2}$:

$$J^{II}_{CO_2} = -\left(\frac{c_T D_{CO_2}}{x_f}\right)\ln\left[1 + \frac{c^o_{O_2} D_{O_2}}{c_T D_{CO_2}}\right] \tag{12}$$

Equation (12) is useful because it helps us derive an expression for L/x_f. At the boundary between Regions I and II, we have the following continuity expressions:

$$J^{II}_{CO} = -2 J^{I}_{O_2} \qquad J^{I}_{O_2} = J^{II}_{CO_2} \tag{13}$$

Upon substitution into equation (12) for $J^{II}_{CO_2}$, we can get the expression for L/x_f:

$$\frac{L}{x_f} = 1 + \frac{c^o_{O_2} D_{O_2}}{c_T D_{CO_2}}\ln\left[1 + \frac{c^o_{O_2} D_{O_2}}{c_T D_{CO_2}}\right] \tag{14}$$

For a system with a constant $\frac{c^o_{O_2}}{c_T}$, such as air where $\frac{c^o_{O_2}}{c_T} = 0.21$, the value for L/x_f is 2.123.

Calculation of Concentration Profiles and Concentrations at Boundaries

First consider the concentration profiles for Region (I). Equation (8) indicates that the concentration profile for CO_2 is linear. Since the flux of O_2 is simply the negative of the CO_2 flux, the concentration profile of O_2 is also linear. These are shown in Figure 2.

The concentration profiles of CO and CO_2 in Region II can be calculated as follows:

$$J^{II}_{CO} = -D_{CO}\left(\frac{\partial c_{CO}}{\partial x}\right) + \frac{c_{CO}\left(J^{II}_{CO} + J^{II}_{CO_2}\right)}{c_T} \tag{15}$$

This can be simplified and integrated to:

$$J''_{CO} = -\left(\frac{2c_T\, D_{CO}}{x_f}\right)\ln\left[\frac{\left(2c_T - c^{\bullet\bullet}_{CO}\right)}{\left(2c_T - c^{\bullet}_{CO}\right)}\right] \tag{16}$$

Noting that $c^{\bullet\bullet}_{CO} \rangle\rangle c^{\bullet}_{CO}$ and combining with equations (13) and (14), we get a concentration function:

$$c^{\bullet\bullet}_{CO} = 2c_T\left[1 - \left(1 + \frac{c^{o}_{O_2}\, D_{O_2}}{c_T\, D_{CO_2}}\right)\right]^{-D_{CO_2}/D_{CO}} \tag{17}$$

This equation gives the reduction in concentration of CO in Region (II). According to equation (13) the flux of CO_2 has the opposite sign and twice the magnitude at any given point. These concentration profiles are shown in Figure 2(b).

Calculation of Recession Rate

The weight loss of carbon per unit area of pinhole is given by:

$$\frac{dW_c}{dt} = M_c\, J'_{CO_2} = \frac{M_c\, c^{o}_{O_2}\, D_{O_2}}{\left(L - x_f\right)} = \frac{M_c\, P_{O_2}\, D_{O_2}}{RT\left(L - x_f\right)} \tag{18}$$

Here W_c is the weight of carbon (gr), M_c is the molecular weight of carbon (gr/mole), and P_{O_2} is the partial pressure of oxygen (bar). The weight loss rate per pinhole is simply this quantity times the area of the pinhole, πr^2. The rate of growth of a hemisphere at the bottom of the pinhole is given by:

$$\frac{dW_c}{dt} = \rho \frac{dV}{dt} = \rho \left[\frac{d\left(\frac{2\pi s^3}{3}\right)}{dt} \right] \tag{19}$$

where s is the radius of the underlying hemispherical void, V is the volume, and ρ is the density of carbon. Equation (19) can be equated to equation (18) and solved for the hemispherical radius, s:

$$s = \left(\frac{3W_c t}{2\pi \rho}\right)^{1/3} = \left[\frac{3r^2 M_c P_{O_2} D_{O_2} t}{2\rho RT(L - x_f)}\right]^{1/3} \tag{20}$$

Functional Dependence of Cavity Growth Rate

Table IV summarizes the dependence of cavity oxidation rate on various parameters. The hemispherical geometry of the cavity leads to the $(\text{time})^{1/3}$ dependence for radius increase. Only a slight temperature dependence is expected for a diffusion-controlled process. The independence on total pressure results from the fact that the pressure terms always appear as a ratio $P(O_2)/P(\text{Total})$. This ratio remains constant in the situation discussed. If, however, the amount of oxygen in the atmosphere changes, then the oxidation rate would change. A change in this ratio would also change L/x_f, as indicated by equation (14). The dependence on pinhole geometry follows from equation (20). Note the significant dependence on pinhole radius.

Comparison of Theory to Experiment

Table II lists theoretical pinhole weight changes calculated from the diffusion-limited models for each condition. A comparison of theory to experiment indicates the effectiveness of the model. The major source of error in these calculations is the determination of the pinhole radius. As shown in Figures 3b, 5-8, and 11 the difficulties in ultrasonically drilling such a small hole leads to non-uniform pinhole radii and variations from hole to hole. This is important since the calculated weight loss varies as the square of the pinhole radius, as discussed above. An average pinhole radius of 0.02 cm was taken for these calculations. The pinhole length tended to be more uniform

and was taken as 0.08 cm. Uncertainties also arise from the weight losses of the specimen without pinholes (Table I).

Given these uncertainties, agreement is considered reasonable for the two higher temperature furnace exposures, but not at the 600°C furnace exposure. Visually, there was little attack of the carbon (Figure 5) and the small weight gain is due to the variation in weight loss between the blank and the pinhole specimen. At the lower temperatures, the shortfall of the measured weight changes compared to the diffusion theory predictions suggests that the process is not solely diffusion controlled but may be influenced by the surface reaction of carbon and the oxidant. The selective attack illustrated in Figure 9 further supports surface reaction control of the overall process.

The weight loss for the arc-jet experiment increases with time, although it is not truly linear as the model predicts. The amount of carbon oxidized is substantially more than that predicted from the model. It is likely that the diffusion equations do not adequately describe the effects on gas transport in the pinhole from the external high velocity stream.

Summary

one dimensional

The oxidation through pinholes in a SiC-protected carbon/carbon material has been investigated. Experimental pinholes were drilled through the SiC coating and oxidation damage was quantified by both weight changes and the examination of cross-sections. A diffusion-control model for carbon oxidation was developed to describe this oxidation process. Agreement between the experimental measurements and theoretical calculations for the 1000 and 1400°C exposures is reasonable, supporting diffusion control. At 600°C the process appears to be controlled by a surface reaction.

quiescent

Acknowledgments

We wish to express our appreciation to Ge Wang and Xuejin Zheng, formerly of The Ohio State University, for their assistance with the calculations. The assistance of D. Humphrey, NYMA/NASA Lewis Group is also appreciated.

Table I. Weight loss of Blank--C/C Specimen (all in mg)

Temperature (°C)	5 torr	70 torr
600	-14.45 +/- 1.63	-15.99 +/- 4.29
1000	-14.94 +/- 6.68	-8.63 +/- 2.32
1400	-28.62 +/- 5.53	-24.79 +/- 8.60

Table II. Exposure Conditions and oxidative attack for each pinhole

Sample	Exposure Time (hr)	Exposure Temperature (°C)	Exposure Pressure (bar)	Average, measured weight change (mg)	Measured cavity area (mm^2)	Weight Change calculated from cavity area (mg)	Weight change calculated from diffusion model (mg)
PH2	1	1400	0.0066	-3.36 +/- 0.61	1.20 +/- 0.37	-1.91 +/- 0.33	-7.7
PH3	1	1600	0.0066	-68.831			
PH4	1	1400	0.092	-7.48 +/- 0.96	2.64 +/- 0.56	-6.22 +/- 0.61	-7.7
PH5	1	1000	0.092	-1.67 +/- 0.26	0.94 +/- 0.69	-1.32 +/- 0.83	-6.1
PH6	1	1000	0.0066	-1.78 +/- 0.74	1.15 +/- 0.57	-1.79 +/- 0.62	-6.1
PH7	1	600	0.0066	+0.09 +/- 0.48		0	-4.8
PH8	1	600	0.092	+0.16 +/- 0.18		0	-4.8
AJ1	3.5	1538	0.050	-210	17.5 +/- 11	-106 +/- 53	-27

Table III. Diffusivities of O_2 in nitrogen (cm^2/sec) determined from Chapman-Enskog correlation.

Temperature (°C)	0.0066 bar	0.092 bar
600	192	13.8
1000	358	25.7
1400	573	41.1
1538		46.3

Table IV. Dependence of cavity growth rate on various parameters.

Parameter	Dependence of Cavity Weight Loss	Dependence of Cavity Radius
Time	$\propto t$	$\propto t^{1/3}$
Temperature	$\propto T^{1/2}$	$\propto T^{1/6}$
Pressure	Independent	Independent
Partial Pressure of Oxygen	$\propto P_{O_2}$	$\propto P_{O_2}^{1/3}$
Pinhole radius	$\propto r^2$	$\propto r^{2/3}$

References

1. S. D. Williams, D. M. Curry, D. C. Chao, and V. T. Pham, AIAA 94-2084, 6th AIAA/ASME Joint Thermophysics and Heat Transfer Conference, June 20-23, 1994, Colorado Springs, CO.

2. M. E. Westwood, J. D. Webster, R. J. Day, F. H. Hayes, and R. Taylor, Oxidation Protection for Carbon Fibre Composites, J. Mat. Sci. 31, 1389-1397 (1996).

3. N. S. Jacobson and R. A. Rapp, NASA TM 106793, 1995.

4. J. M. Thomas, "Microscopic Studies of Graphite Oxidation", pp. 121-202 in Chemistry and Physics of Carbon, ed. by P. L. Walker, Marcel Dekker, Inc., New York, 1965.

5. K. L. Luthra, Carbon 26 [2], 217-224 (1988).

6. J. Bernstein and T. B. Koger, *J. Electrochem. Soc.* 135 [8], 2086-2090 (1988).

7. E. L. Courtright, J. T. Prater, G. R. Holcomb, G. R. St. Pierre, and R. A. Rapp, *Oxid. Met.* 36 [5/6], 423-437 (1991).

8. G. R. Holcomb and G. R. St. Pierre, *Oxid. Met.* 40 [1/2], 109-118 (1993).

9. L. Filipuzzi, G. Camus, R. Naslain, and J. Thebault, *J. Am. Ceram. Soc.* 77 [2], 459-66 (1994).

10. L. Filipuzzi and R. Naslain, *J. Am. Ceram. Soc.* 77 [2], 467-80 (1994).

11. A. J. Eckel, J. D. Cawley, and T. A. Parthasarathy, *J. Am. Ceram. Soc.* 78 [4], 972-80 (1995).

12. G. R. Holcomb, *Corrosion* 52 [7], 531-539 (1996).

13. S. V. Christensen, "Reinforced Carbon/Carbon Pin Hole Formation through Zinc Oxide Attack," May 1996.

14. G. H. Geiger and D. R. Poirier, Transport Phenomena in Metallurgy, Addison-Welsey Publishing Company, Reading, MA, 1973.

15. R. A. Svehla, "Estimated Viscosities and Thermal Conductivities of Gases at High Temperatures," NASA Technical Report R-132.

16. T. K. Sherwood, R. L. Pigford, and C. R. Wilke, Mass Transfer, McGraw-Hill, New York, 1975, p. 20.

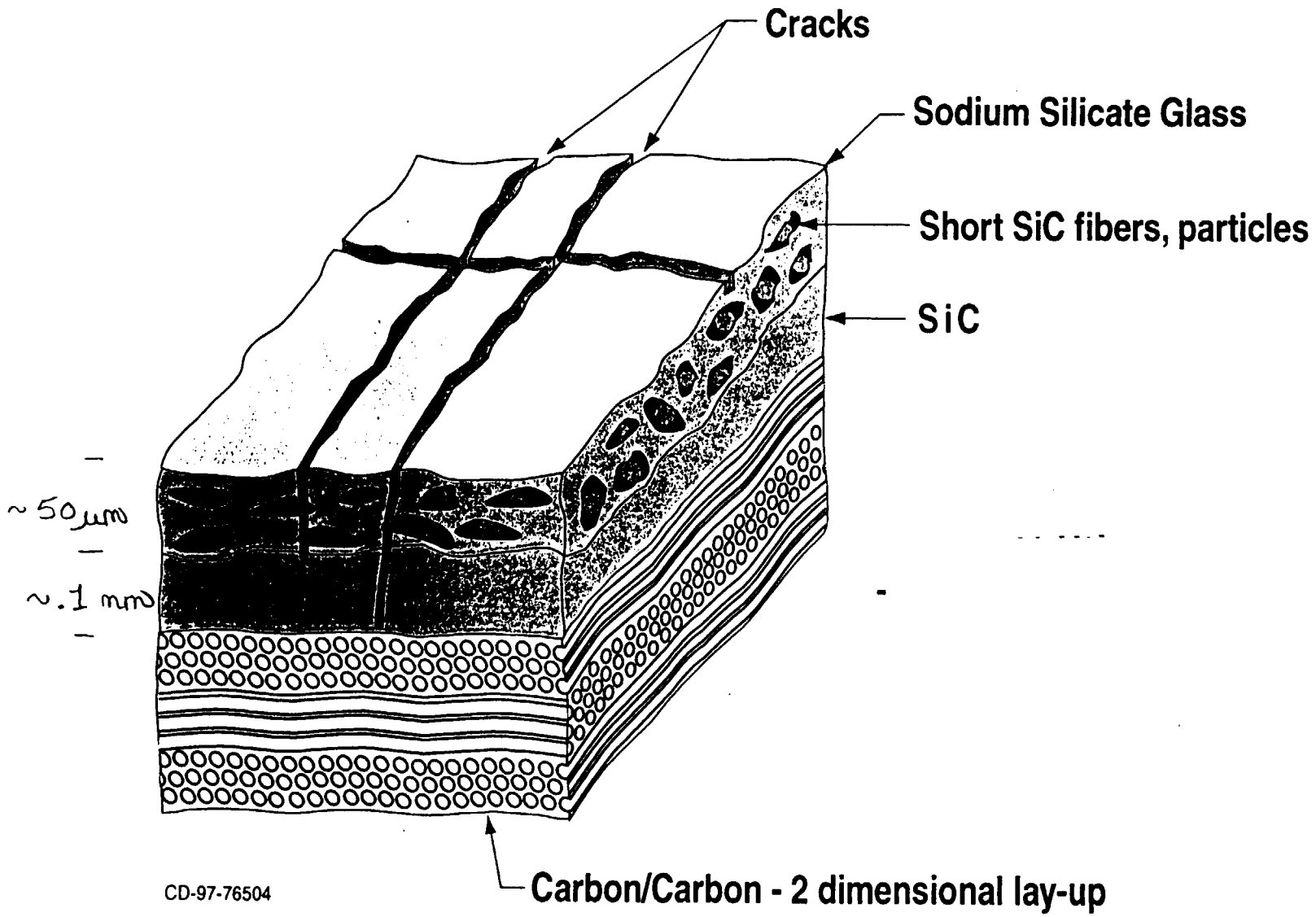
Cracks
Sodium Silicate Glass
Short SiC fibers, particles
SiC
~50 μm
~.1 mm
CD-97-76504
Carbon/Carbon - 2 dimensional lay-up

Fig 1

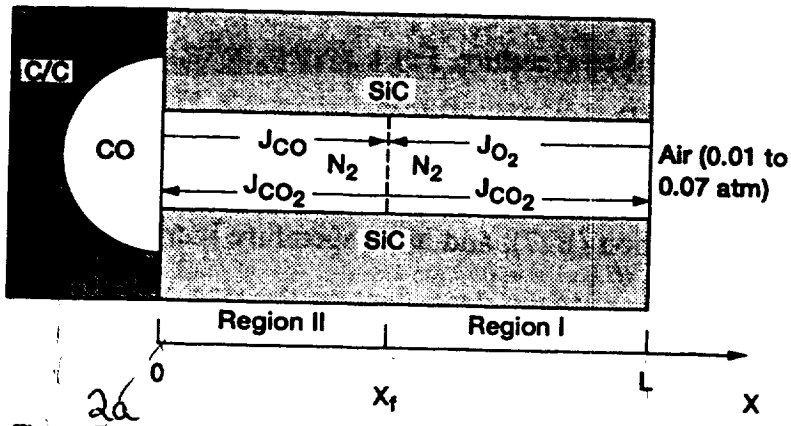

Figure 2a.-

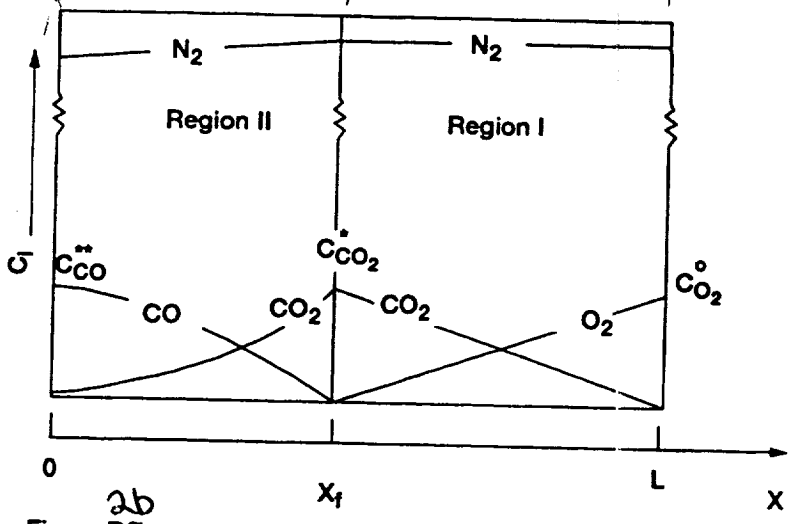

Figure 2b.-

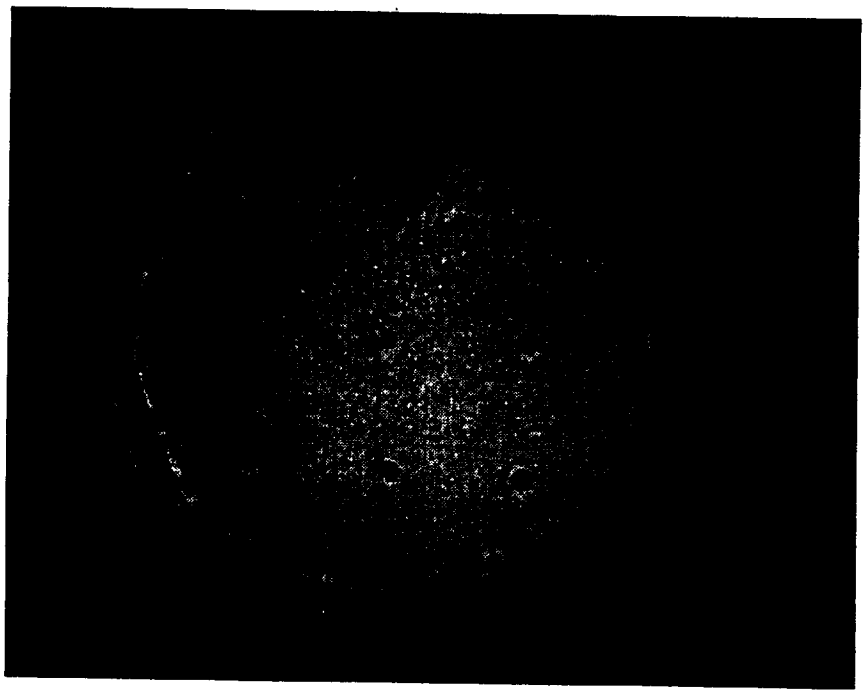

Fig 3a

3.3 mm

CD-97-75355

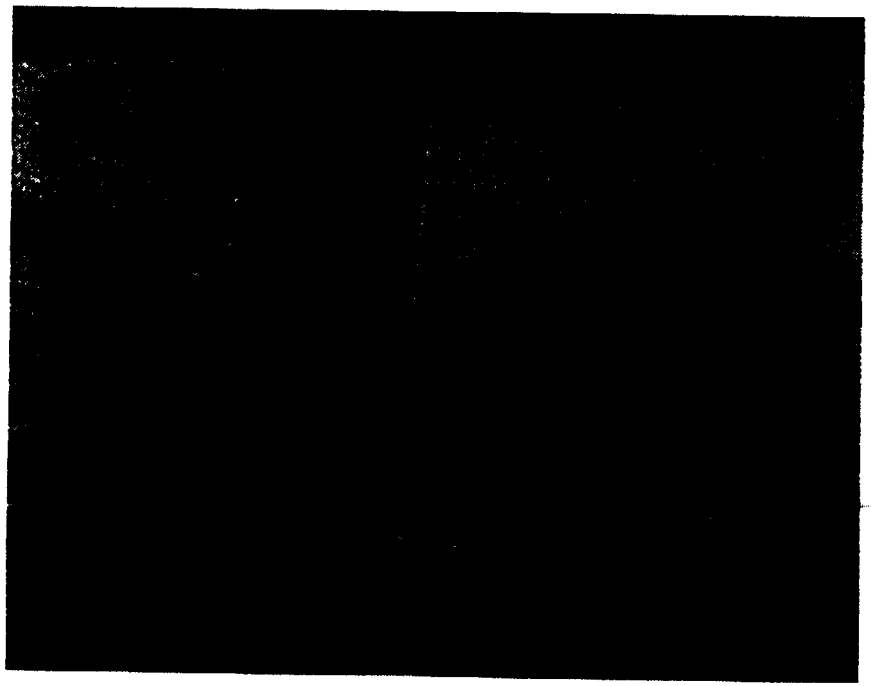

0.4mm

Fig 3b

CD-97-75354

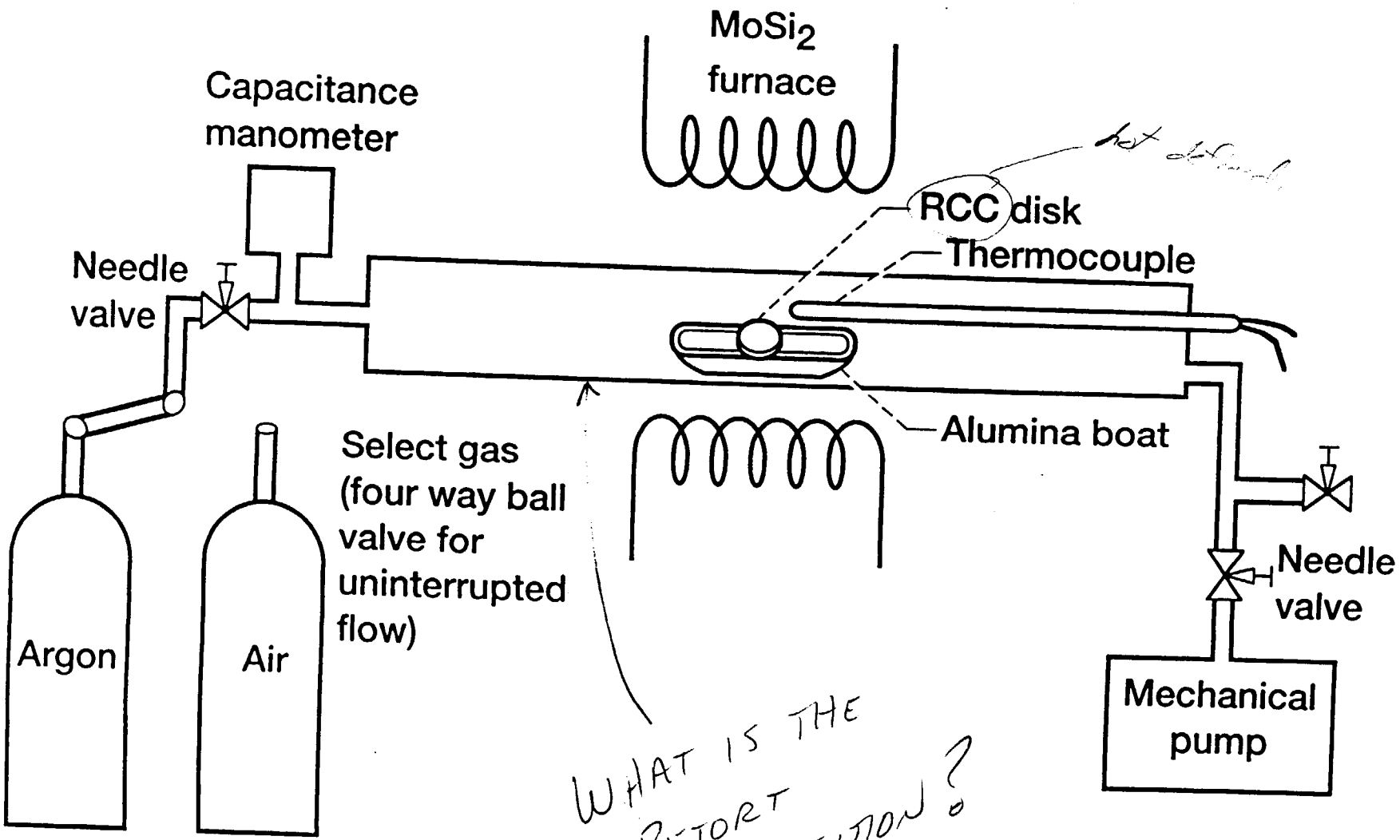

Fig 4

CD-96-72559

0.4 mm

Fig 5

CD-97-75358

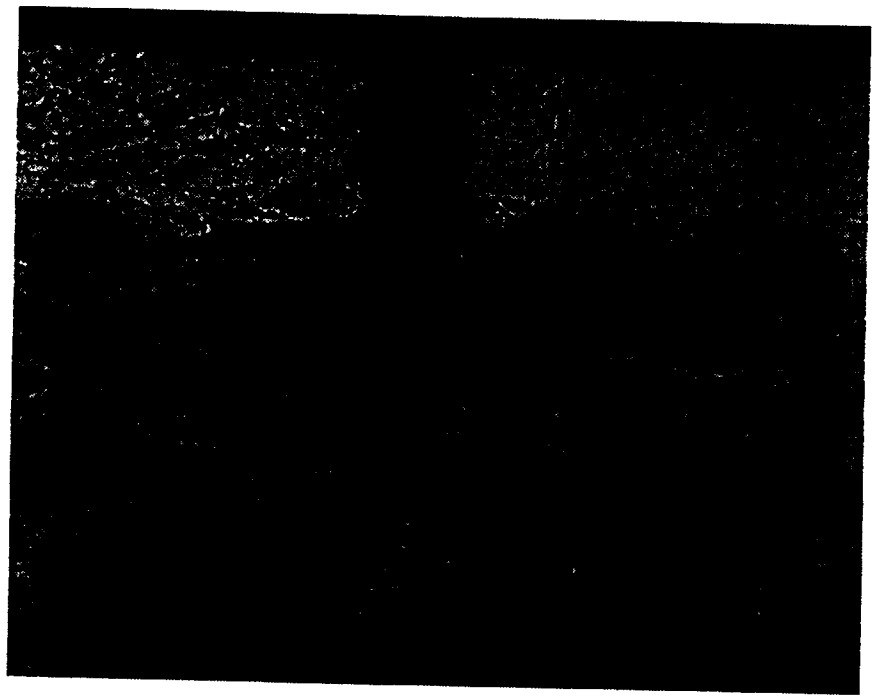

0.4 mm

Fig 6

CD-97-75356

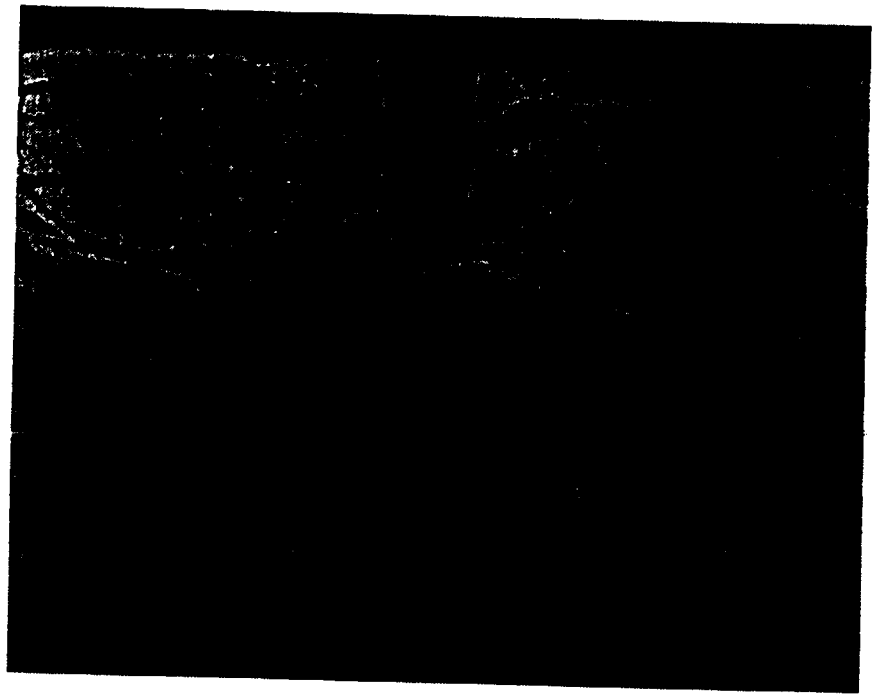

0.4mm

Fig 7

CD-97-75357

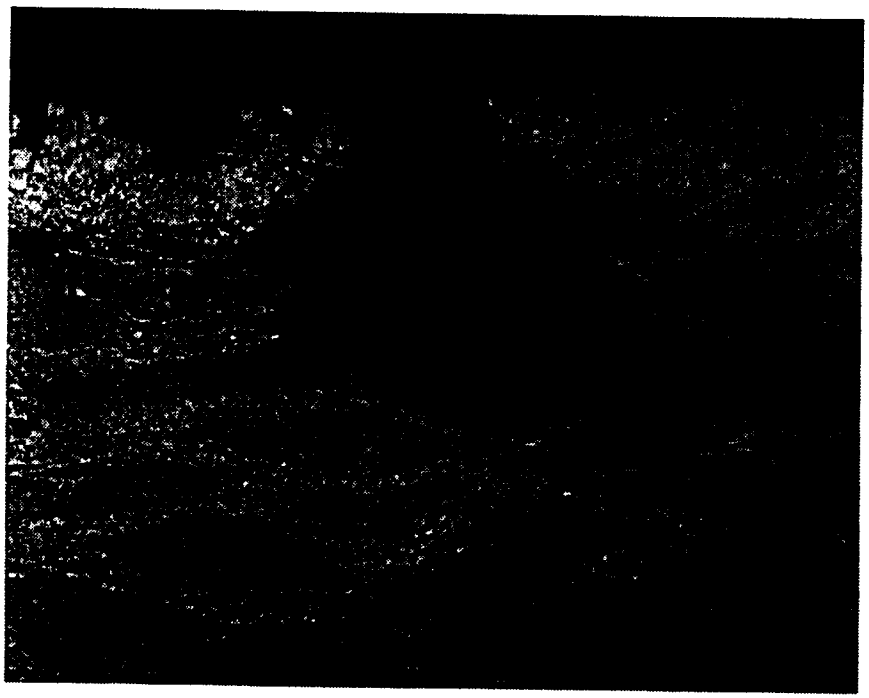

0.4mm

CD-97-75359

Fig 8

Fig 9.

Can you show me where this image is from in Fig. 5?

0.1mm

Fig 9

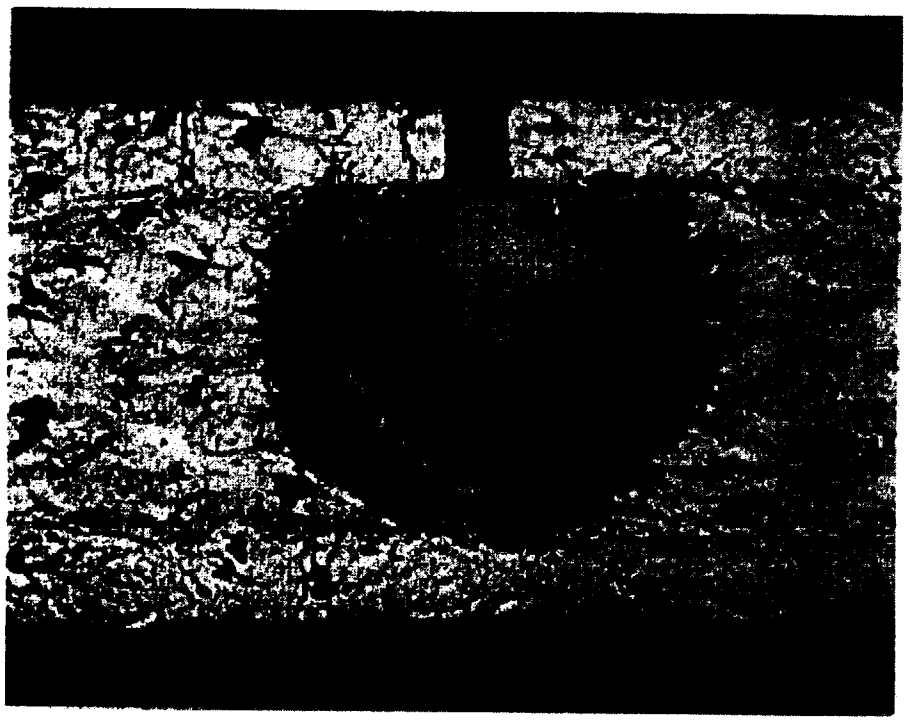

Fig 11

1 mm

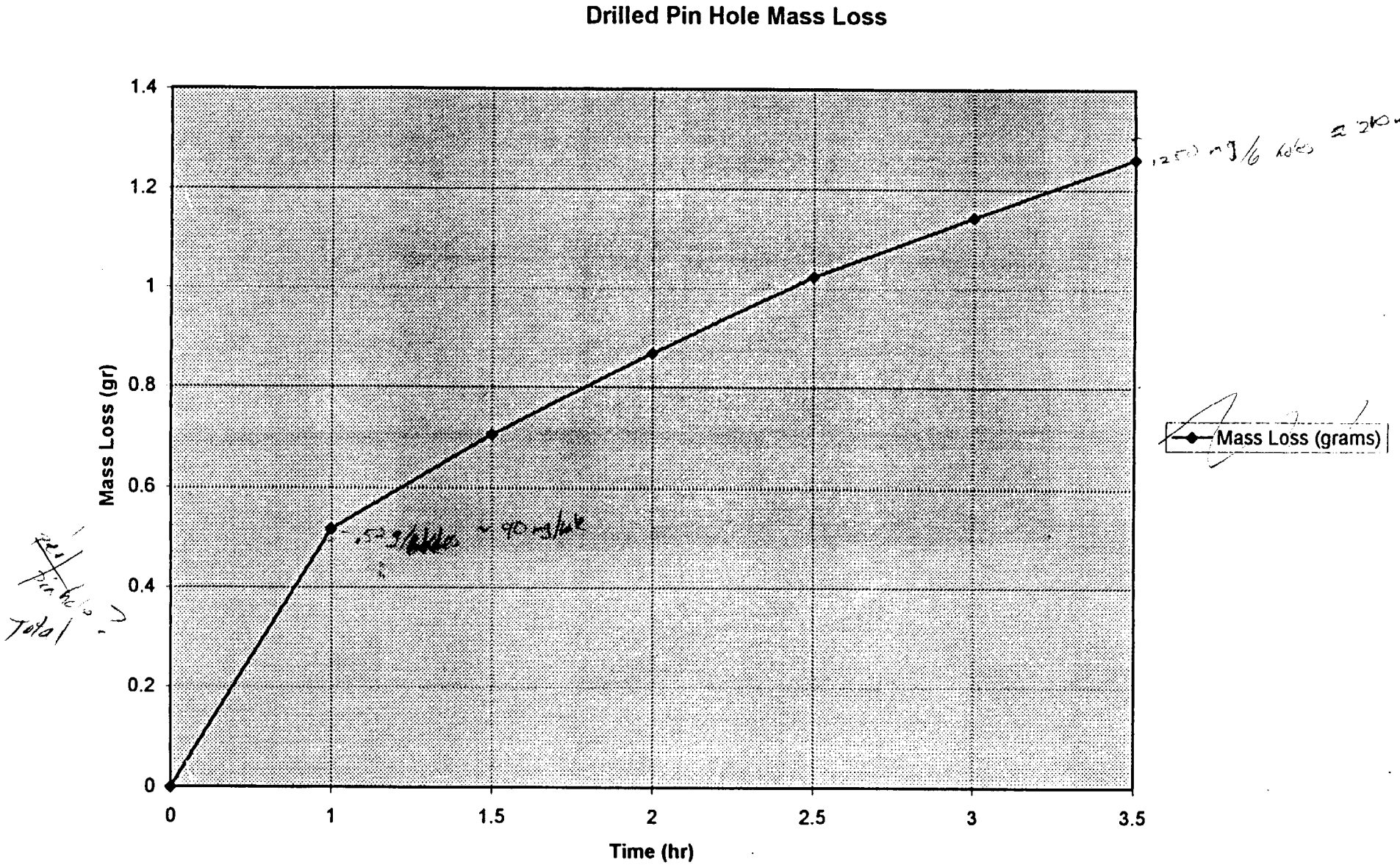
Drilled Pin Hole Mass Loss
Mass Loss (gr)
1.4
1.2
1
0.8
0.6
0.4
0.2
0
0
1
1.5
2
2.5
3
3.5
Time (hr)
Mass Loss (grams)

Fig 10

Fig 11

1 mm